Discrepancy in the Aerodynamic Property and Flowfield of a Symmetric Airfoil Produced by the Stationary and Moving Ground Effect

V. Tremblay-Dionne
Department of Mechanical Engineering,
McGill University,
Montreal, QC H3A 2K6, Canada

T. Lee[1]
Department of Mechanical Engineering,
McGill University,
Montreal, QC H3A 2K6, Canada
e-mail: tim.lee@mcgill.ca

The discrepancy in the aerodynamic property and flowfield of a symmetric airfoil produced by the stationary and moving ground effect was quantified through surface pressure and particle-image-velocimetry measurements. The results show that the stationary ground effect produced a higher lift than the moving ground due to the flow passage restriction caused by the longitudinal boundary layer developed on its ground surface. In close ground proximity, the formation of a ground vortex beneath the airfoil's leading-edge region speeded up the flow, leading to a lower lift than its moving-ground counterpart. For the moving ground, the ground vortex was absent. In close ground proximity, the moving ground effect generated a larger wake and drag than the stationary ground effect. [DOI: 10.1115/1.4048290]

1 Introduction

For aircraft flying close to the ground, especially during takeoff and landing, the pilots always experience an unwanted extra lift or the so-called "floating." On the other hand, the ground effect-induced lift increase and lift-induced drag reduction have been utilized in winged ground-effect vehicles. In ground effect, the lift increase is produced by the ram pressure, or dynamic air cushion, developed in the narrowed flow passage between airfoil's lower surface and the ground surface, which is referred to as the chord-dominated ground effect. For finite wings, the ground effect-produced lift-induced drag reduction is caused by the suppression of the wingtip vortices and their outboard displacement and is generally referred to as the span-dominated ground effect. Extensive theoretical, numerical, and experimental research effort has been devoted to the aerodynamics and flowfield produced by the chord-dominated [1–16] and span-dominated [17–21] ground effect. However, due to the different ground boundary conditions, Reynolds numbers, airfoil profiles, flow facilities, and analysis methods employed, there is a large scatter in the published ground effect-induced lift and drag forces. To narrow the scope of this study, a brief review of the chord-dominated ground effect is given below. A more detailed review can be found in the work of Barber et al. [1].

Carter [2] investigated the ground-effect aerodynamics by towing the wing model over the water surface. The presence of the ground was found to lead to an increased lift-drag slope and a reduced lift-induced drag while a virtually unaffected profile drag force. Turner [3] observed a fairly drastic effect on the airfoil's sectional lift coefficient C_l as the fixed ground was approached. A 33% increase in C_l was obtained at a ground height of 33% of the span. Suh and Ostowari [4] showed that the ground proximity led to a reduced sectional drag coefficient C_d, an increased C_l/C_d ratio, as well as an increased flow separation. Steinbach and Jacob [5] simulated the moving ground (MG) condition by the removal of the boundary layer developed on a fixed ground through a suction system. They also found that in ground effect, the flow separation was enlarged, and that the lift was increased with decreasing ground clearance while the drag was decreased. No flowfield information and ground effect-produced pitching moment coefficient C_m were reported by these investigators [2–5].

Hayashi and Endo [6] examined the fixed ground effect on the wake of a NACA 4412 airfoil at an angle of attack $\alpha = 15$ deg and a chord Reynolds number $\mathrm{Re} = 3.2 \times 10^5$ both experimentally and numerically. They found that the wake region was enlarged and that the flow separation occurred much earlier than the out of ground effect (OGE) counterpart. Hsiun and Chen [7] simulated the aerodynamics of an NACA 4412 airfoil in fixed ground effect for $\alpha \leq 10$ deg at $\mathrm{Re} = 3.2 \times 10^5$. They also found that the flow separation was stronger than the OGE case, and that the values of C_l and C_d were a strong function of the ground clearance. Steinbach [8] further suggested that the more suitable boundary condition for the ground plane should be the slip condition. The boundary layer developed on the fixed ground can affect the lift results for a ground distance $h \leq 5\%$ chord.

Moore et al. [9] measured the C_l and C_d of a NACA 0012 wing with an aspect ratio $\mathrm{AR} = 3.01$ in a rolling road wind tunnel for $\mathrm{Re} \leq 8 \times 10^5$. Both C_l and C_d were found to increase with the decreasing h/c value. They also noticed a reduction in C_l in ground proximity for $\alpha \leq 3$ deg due to the suction effect developed on the airfoil's lower surface, as a result of the convergent-divergent passage developed between the airfoil and the ground surface. Furthermore, there was little difference between the drag values when the moving ground surface was turned off. Moore et al. further divided the ground effect into two distinct regimes: ram and normal ground effect. The ram ground effect occurs for $h/c \leq 10\%$ for which an almost sealed envelope is created between the wing's trailing edge and the ground surface. For $h/c > 10\%$, the wing enters what is normally considered to be normal ground effect.

Barber et al. [1] investigated the aerodynamics and flowfield of a finite NACA 4412 wing in ground effect both numerically and

[1]Corresponding author.

Contributed by the Fluids Engineering Division of ASME for publication in the Journal of Fluids Engineering. Manuscript received June 12, 2020; final manuscript received August 17, 2020; published online October 26, 2020. Assoc. Editor: Hui Hu.

experimentally. Their computational fluid dynamics simulation showed that there was a large C_l discrepancy in close ground proximity between moving and fixed ground effect at $\mathrm{Re} = 8.2 \times 10^6$ and $\alpha = 2.9$ deg, while only a small C_l difference existed for $h/c > 10\%$. A recirculation region in the ground stationary model was also visible beneath the airfoil's leading edge from the calculated velocity profiles at $h/c = 2.5\%$. Their computational fluid dynamics results were also supported by limited particle image velocimetry (PIV) flowfield measurements at $\mathrm{Re} = 6.1 \times 10^4$ in a channel flow. They also concluded that

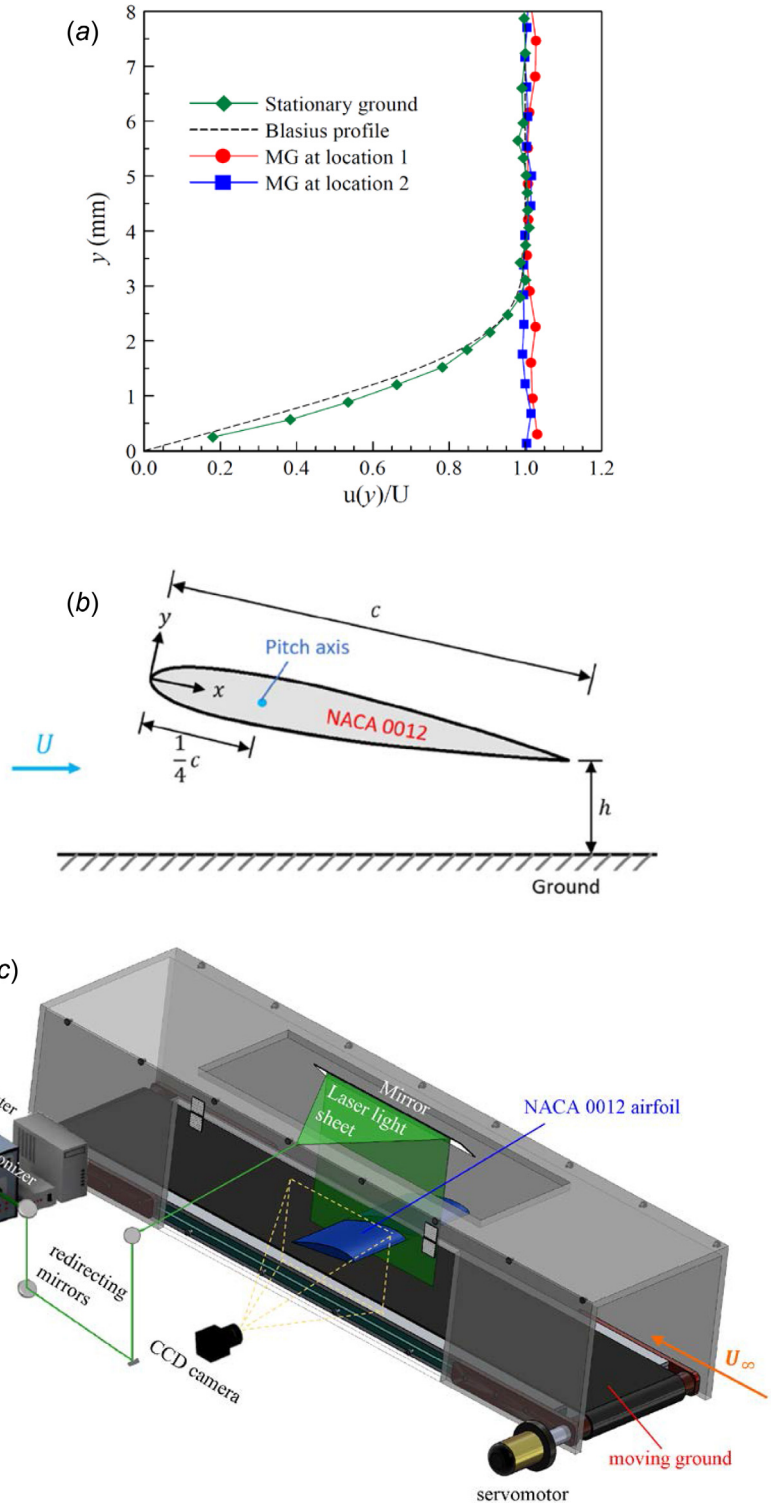

Fig. 1 (*a*) Boundary-layer velocity profiles developed on the elevated flat plate and MG, (*b*) airfoil model and definition of ground distance or clearance *h*, and (*c*) schematics of PIV setup and moving ground. MG at location 1 and location 2 denote hot-wire probe located at 5 cm and 30 cm (or at the leading edge of the airfoil) from the beginning of the moving ground surface, respectively.

viscous effects are significant for ground effect flight, and it is therefore unlikely that inviscid solutions will give an accurate representation of ground effect aerodynamics. No aerodynamic coefficients were, however, reported experimentally.

Ahmed and Sharma [10] investigated the flow and aerodynamic characteristics of a NACA 0015 airfoil in fixed ground effect in a wind tunnel. They found that a high surface pressure coefficient C_p appeared on the airfoil's lower surface as the ground was approached, leading to an increased C_l, and that the flow was accelerated over the airfoil due to flow diversion from the lower surface especially for higher α, which resulted in a thicker wake and hence a higher drag. Ahmed et al. [11] investigated experimentally the aerodynamic and flow characteristics of a NACA 4412 airfoil in the moving ground effect at $\mathrm{Re} = 3 \times 10^5$. The C_l was found to increase with decreasing h/c for high α while decrease with reducing h/c for small α. Meanwhile, only a minor loss of upper surface suction exhibited as the airfoil approached the ground for all α. The pressure drag was also found to be higher at small h/c for all α tested, due to the high pressure drag originated from the airfoil lower surface. Their hot-wire measurements also showed a stronger suction effect near the leading edge on the upper surface which gives rise to accelerated flow there. Furthermore, as the flow moved toward the trailing edge, the velocity close to the surface was reduced to overcome the adverse pressure gradient. No direct comparison between the fixed ground and moving ground-produced C_l and C_d was documented.

Luo and Chen [12] investigated the fixed ground effect on the aerodynamics of a NACA 0015 airfoil through load cell and C_p measurements in a wind tunnel at $\mathrm{Re} = 1.87 \times 10^5$. They found that the C_l decreased with h/c reducing from 30% to 15% for $\alpha \leq 6$ deg due to the convergent-divergent channel effect, and that the C_l generally lied within the magnitude estimated from the thin airfoil theory. Most recently, Lee et al. [14] investigated the aerodynamic property of a static and an oscillating NACA 0012 airfoil in the fixed ground effect at $\mathrm{Re} = 9.81 \times 10^4$. For the static airfoil, the ground proximity led to a reduced C_l and an increased nose-up C_m for $\alpha < 6$ deg. For $\alpha > 6$ deg, the C_l and nose-down C_m were increased with reducing h/c. Furthermore, the value of C_d always increased in the ground effect. For the oscillating airfoil, a substantial change in the dynamic-C_l loops, especially during downstroke, occurred for $h/c \leq 30\%$, leading to a greatly reduced C_l-hysteresis compared to the OGE case. The dynamic-stall vortex was also found to be weakened and breaks down earlier with reducing h/c, rendering an enlarged separated flow. Note that Zerihan and Zhang [15,16] also investigated extensively the aerodynamics of an inverted wing in the moving ground effect in a wind tunnel.

As discussed previously, despite the extensive investigations on the chord-dominated ground effect-produced aerodynamics, there existed a large scatter in the ground effect-produced aerodynamic coefficients arising from the ground boundary conditions employed. The objective of this study was to quantify the aerodynamic property produced by both fixed and moving ground boundary conditions in a subsonic wind tunnel at a specific Reynolds number through surface pressure measurements. Particle-image-velocimetry flowfield measurements were also acquired to supplement the observed changes in the aerodynamic property.

2 Experimental Methods

The experiment was conducted in the low-turbulence $30 \times 30 \times 150\,\mathrm{cm}^3$ suction-type wind tunnel at McGill University at $\mathrm{Re} = 9.2 \times 10^4$. The 140 cm long moving ground, covering 94% of the width of the wind tunnel floor, was constructed by using a moving belt and can reach a surface speed of 15 m/s. An optical tachometer was used to ensure correct belt velocity. The fixed ground was obtained by using a 1.6 mm-thick metal plate elevated 2 cm above the turned-off moving belt. The mean streamwise velocity profiles developed over the moving ground, and the elevated flat plate were measured with a 5 μm-diameter normal hot-wire probe operated by a constant-temperature anemometer (AA Lab model AN-1003). The probe was mounted on a vertical computer-controlled traversing mechanism and was moved with accuracy in the y direction with 25 μm. Figure 1(*a*) shows that over the fixed ground, a laminar boundary layer, resembling the Blasius velocity profile, was obtained. For the moving ground, the flow remained nearly uniform as it approached the moving ground plane, especially at location 2 which corresponds to the leading edge of the airfoil.

For surface pressure measurement, a rectangular aluminum NACA 0012 wing model, with $c = 12.5$ cm and a span $b = 29.8$ cm, equipped with 48 0.35 mm-diameter pressure orifices was employed. The pressure orifices were connected to a 48-port Scanivalve system in conjunction with a pressure transducer (Type YQCH-250-1) via 22 cm long and 0.75 mm i.d. plastic tubing. The pressure orifices, distributed over the upper and lower surface of the model, were staggered 1.5 mm apart in the streamwise direction to avoid the wake effect from an upstream orifice on orifices further downstream. The pressure orifices were located along the midspanwise position of the wing model. The reference pressure of the transducer was ambient atmospheric pressure measured from inside a fiberglass covered damping unit. The

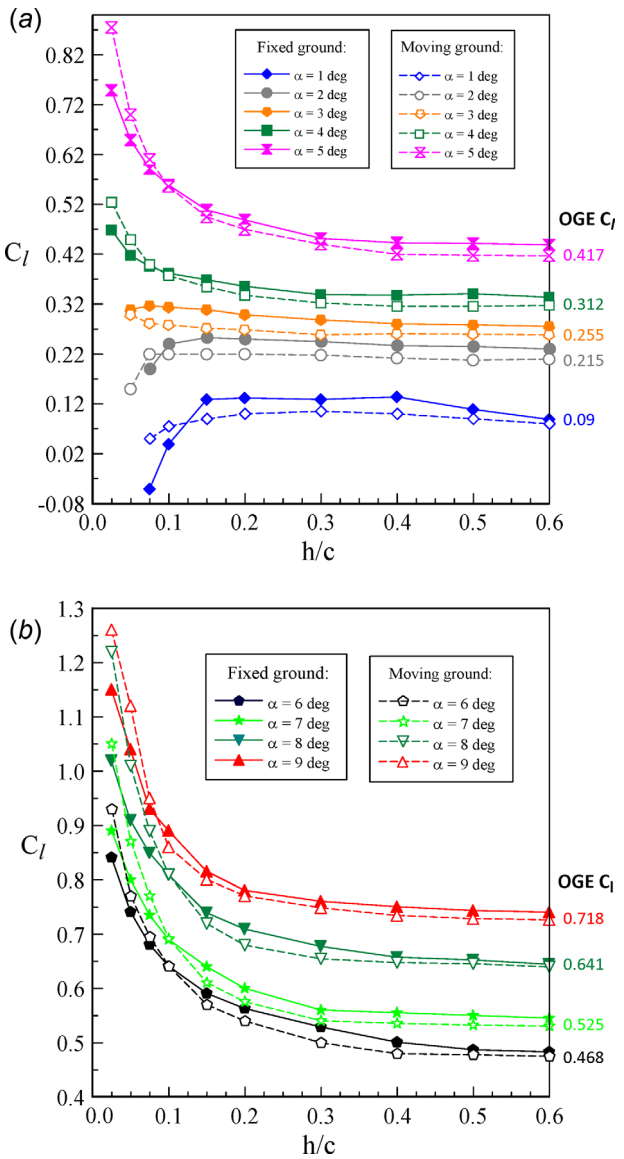

Fig. 2 Effect of the ground boundary condition on C_l as a function of α and h/c

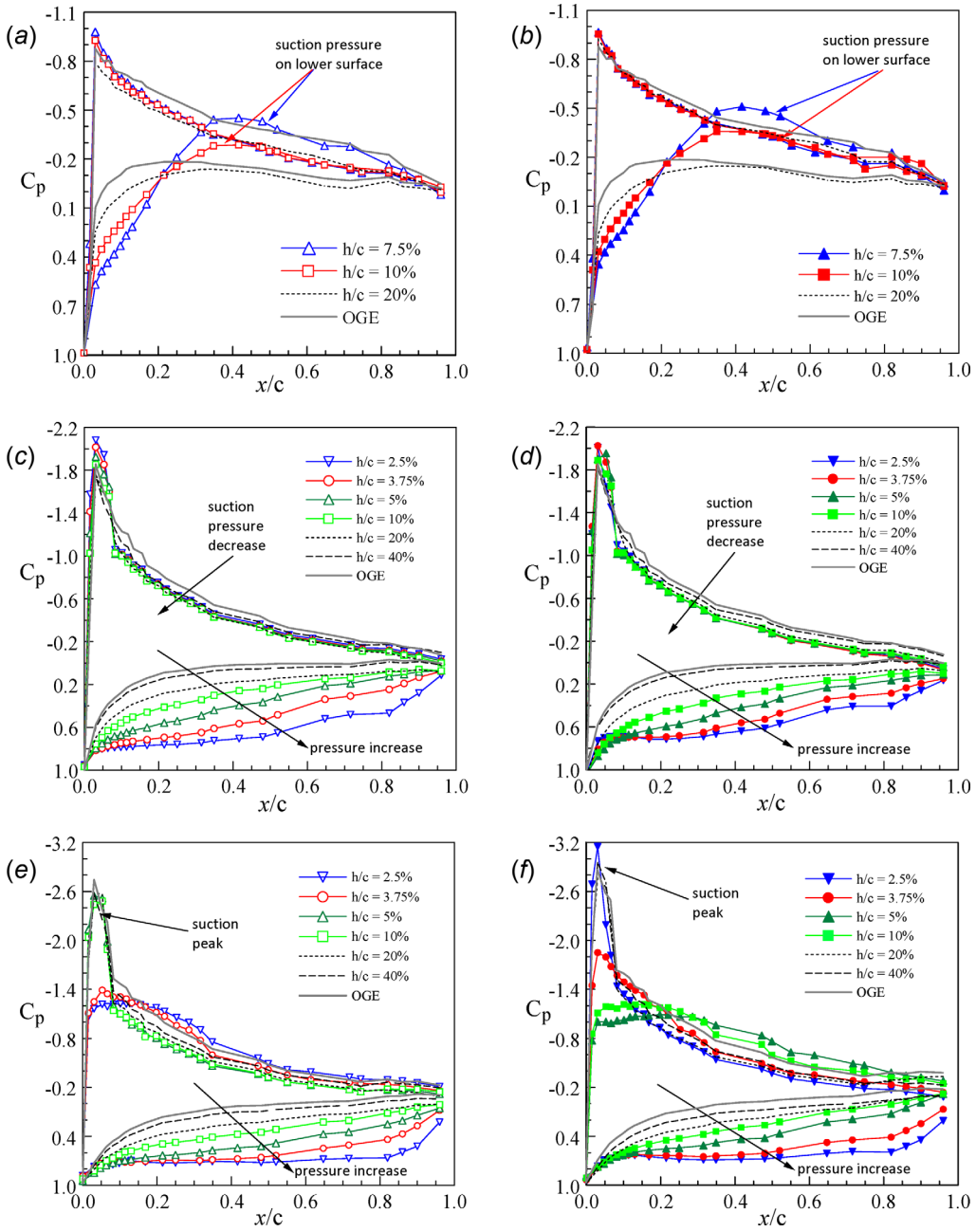

Fig. 3 C_p distribution at selected α and h/c. Moving ground: (*a*) $\alpha = 1$ deg, (*b*) $\alpha = 6$ deg, and (*c*) $\alpha = 9$ deg. Fixed ground: (*d*) $\alpha = 1$ deg, (*f*) $\alpha = 6$ deg, and (*g*) $\alpha = 9$ deg.

output of the pressure transducer was connected to a custom-built signal conditioner, which consisted of an analog signal differential amplifier with gain of 5:1 and an external direct current offset. The pressure transducer calibration has a 99.8% linearity of calibration curve-fit, and the sensitivity is ±5 mV or 62.5 Pa/V, which corresponds to ±0.312 Pa uncertainty or an estimated ±2% uncertainty of the C_p measurement. The signal conditioner output was connected to a data acquisition system and monitored using an oscilloscope. Data were acquired using a 16-channel, 16-bit NI-6259 A/D board powered by a Dell Dimension E100PC. Pressure transducer output was connected to the A/D board via a NI BNC-2110 connector box. Output voltages were sampled at 100 Hz for 10 s in order to obtain a reliable average for recording. The details of the calibration and uncertainty estimation can be found in Ref. [22].

The origin of the coordinates was located at the airfoil's leading edge. The airfoil was pitched at $^1/_4$-chord location. The C_l and C_d were obtained through the integration of the surface pressure distribution around the airfoil via $C_l = \int_{\mathrm{LE}}^{\mathrm{TE}} C_p \sin\theta = \int_{\mathrm{LE}}^{\mathrm{TE}} [C_{p,\mathrm{lower}}(\frac{x}{c})\sin\theta - C_{p,\mathrm{upper}}(\frac{x}{c})\sin\theta] d(\frac{x}{c})$ and $C_d = \int_{\mathrm{LE}}^{\mathrm{TE}} C_p \cos\theta = \int_{\mathrm{LE}}^{\mathrm{TE}} [C_{p,\mathrm{lower}}(\frac{x}{c})\cos\theta - C_{p,\mathrm{upper}}(\frac{x}{c})\cos\theta] d(\frac{x}{c})$ where TE and LE denote trailing edge and leading edge of the airfoil, respectively, and θ denotes the angle between the chord line and the local surface normal vector. The ground distance or clearance is defined as the distance between the airfoil's trailing edge and the ground surface (Fig. 1(*b*)). Different ground distances were obtained by positioning the wing model at desired locations for $h/c = 2.5\%$ to 60% and $\alpha = 1$ deg to 9 deg. Note that in the present experiment, only the pressure drag component was obtained, and the skin friction was not included. The sectional drag coefficient reported here is therefore somewhat underestimated. The aerodynamic properties of the baseline airfoil or OGE airfoil were also obtained to serve as a comparison.

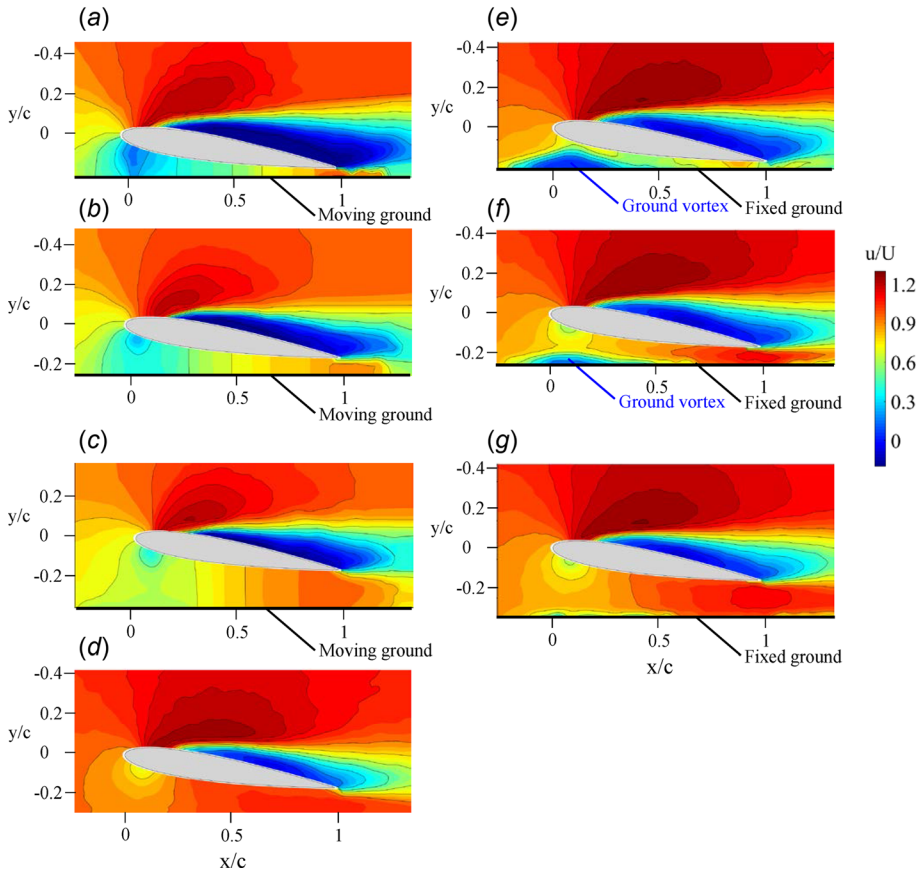

Fig. 4 Impact of ground boundary condition on the iso-u/U contour at $\alpha = 8$ deg. Moving ground: (*a*) $h/c = 5\%$, (*b*) $h/c = 10\%$, and (*c*) $h/c = 20\%$. Fixed ground: (*e*) $h/c = 5\%$, (*f*) $h/c = 10\%$, and (*g*) $h/c = 20\%$. (*d*) OGE.

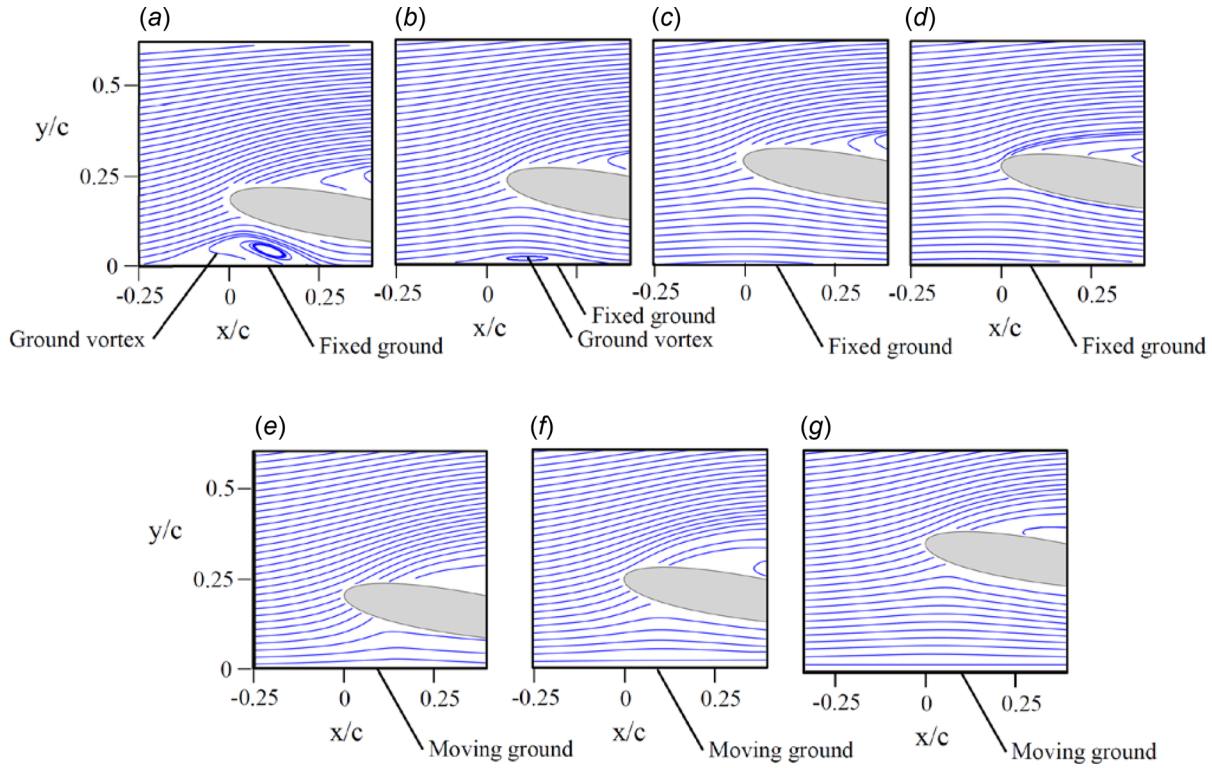

Fig. 5 Streamline pattern in the leading-edge region of the airfoil at $\alpha = 8$ deg. See Fig. 4 for figure caption.

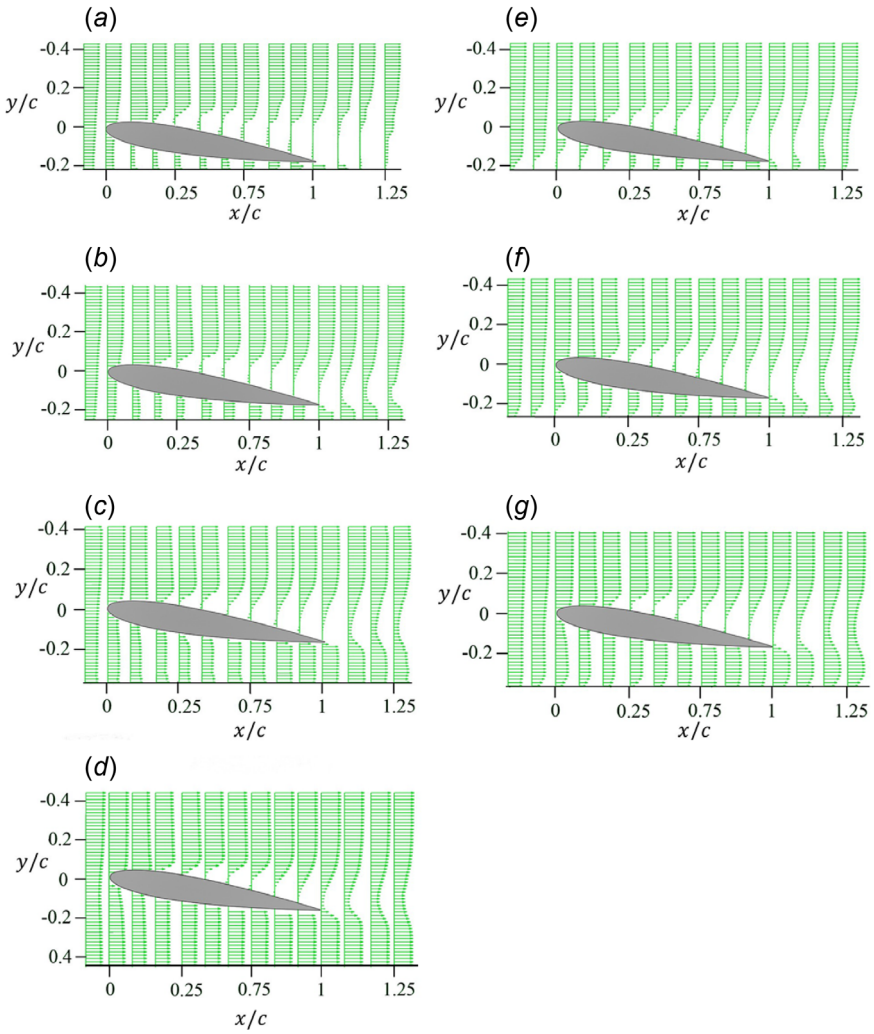

Fig. 6 Velocity vector plots at $\alpha = 8$ deg. See Fig. 4 for figure caption.

For the PIV experiment, the center 5 mm section of the wing model was made transparent to allow the passage of the laser light sheets. The flowfield was illuminated by two 1.7 mm-thick laser light sheets, generated by a dual head Continuum Nd:YAG laser (Model SureLite II), pulsed at 10 Hz and separated by a time delay of 49.4 μs. The time separation between the two laser pulses allows the particle to travel a maximum distance of a quarter spot size (size determined by the squared vector resolution) at freestream speed. The 15 cm wide laser sheet was produced by a cylindrical lens. Seeding particles of propylene glycol (Fisher Chemical P355-1, Waltham, MA) measuring 1–3 μm in diameter, according to manufacturer's specifications, were produced by using a TSI 6-jet atomizer (model 9306). The particles were introduced into the flow upstream of the contraction via a custom-built injector. The particle images were digitally acquired by using a TSI PowerView 4 MP Plus charge-coupled device (CCD) camera (model 630059) with a resolution of 2048 × 2048 pixels, a pixel size of 7.4 μm, a 12-bit dynamic range, and a maximum frame rate of 16 Hz, via a 64-bit Coreco Imaging X64-CL frame grabber installed in a HP XW9400 workstation. A 105 mm focal lens (105 mm) at *f*/6 was used to record the field of view at a magnification ratio of 6.1 at *f*/6 aperture. Timing and control of the PIV system, which includes the lasers, CCD camera, frame grabber, and synchronizer, were accomplished by a programmable LaserPulse synchronizer (model 610035) with a time resolution of 1 ns. Calibration of the camera was achieved by placing a ruler in the field of view and associating the distance between two points with the number of pixels between them. Figure 1(*c*) shows the schematics of the PIV system and moving ground setup.

The PIV images were analyzed by using INSIGHT 3G (version 8.0.4.0) software package developed by TSI, Inc. A two-frame cross-correlation analysis of the PIV images was implemented in the computation of the velocity vectors inside the region of interest. A Gaussian curve-fit was implemented to determine the location of the correlation map peak with subpixel accuracy. A multipass scheme was implemented which progressively decreased the size of the interrogation window and adjusted the extent of the image shift based on the previously computed velocity vector. The size of the interrogation window was set to either 24 × 24 or 32 × 32 (representing a physical size of roughly 1.5 and 2 mm, or 2% and 2.6%, respectively), with a 50% overlapping of the interrogation windows. Postprocessing of the velocity fields consisted of first vector validation (i.e., removal of erroneous and noisy vectors), followed by the application of a 3 × 3 Gaussian filter to remove random variations, and finally interpolation of missing vectors. The field of view was 126 mm by 86 mm with a total of 2800 vectors, which gave a vector density of 2.6 vectors/mm^2. The pixels resolution was 102.5 pixels/cm. The ensemble-averaged velocity (over 120 PIV images) was found to be accurate to within 1% of the freestream velocity. The pixels resolution was 102.5 pixels/cm. The PIV system parameters were chosen following the guidelines detailed in Refs. [23–25].

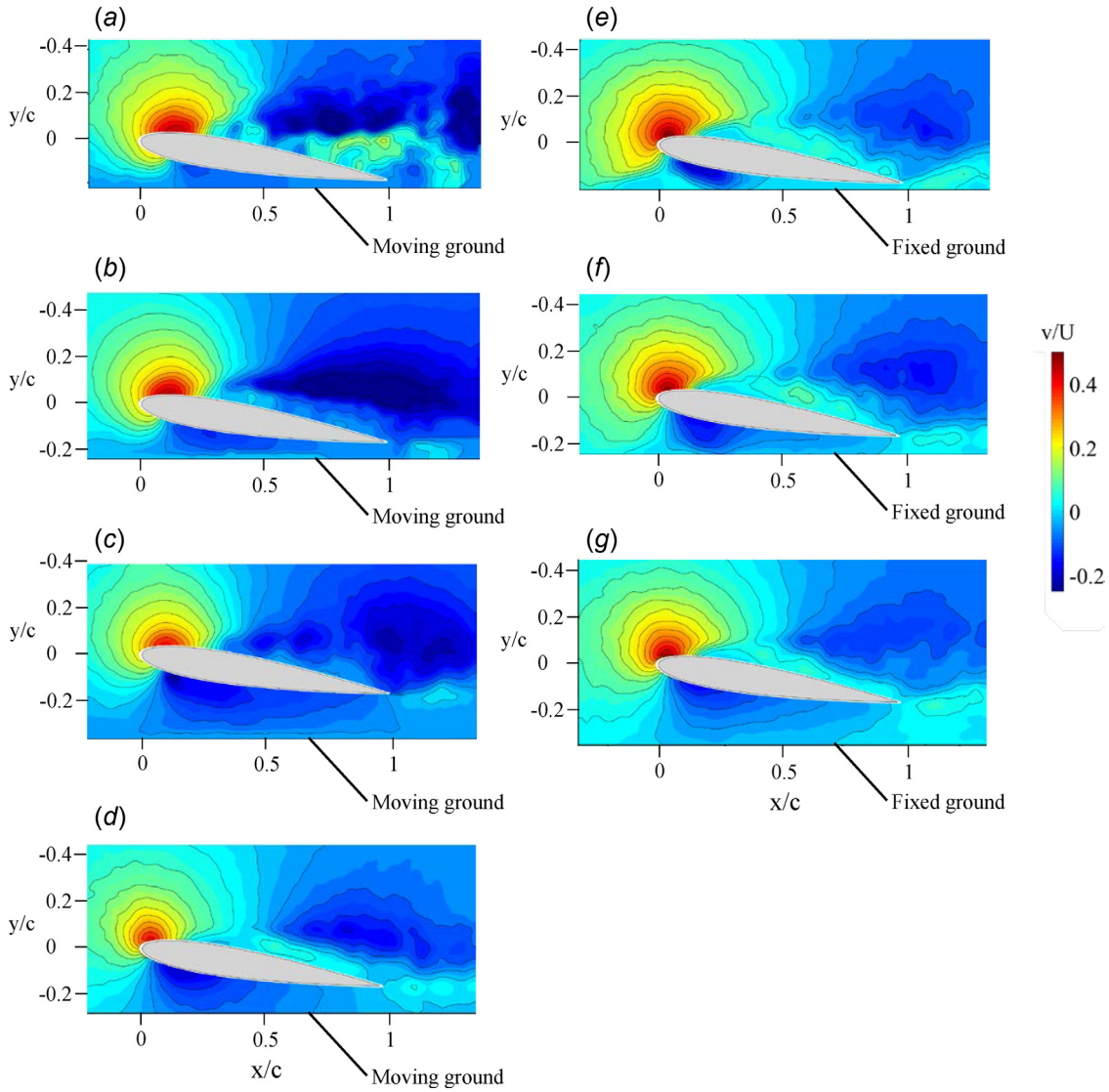

Fig. 7 Iso-v/U contours at $\alpha = 8$ deg. See Fig. 4 for figure caption.

3 Results and Discussion

The discrepancy in the aerodynamic coefficients produced by the fixed and moving ground effects was quantified first, supplemented by the PIV flowfield measurements. For clarity, the C_l and C_d results were presented in two consecutive subfigures.

Figure 2 shows that for both fixed and moving grounds, there was always a C_l increase with reducing h/c for $\alpha > 3$ deg as a result of the ground proximity-created ram pressure. The C_l increased rapidly and nonlinearly for $h/c < 20\%$, and approached the OGE value for $h/c > 60\%$. The fixed ground effect, however, produced a higher C_l than the moving ground for $h/c > 15\%$ but a lower C_l for $h/c < 15\%$. For $\alpha < 3$ deg, there was a drop in C_l with decreasing h/c for $h/c < 15\%$ due to the converging-diverging flow passage developed underneath the airfoil [9], which translates into an unusual suction pressure on the airfoil's lower surface (see Figs. 3(*a*) and 3(*b*)).

Figures 3(*c*) and 3(*d*) indicate that for $\alpha > 3$ deg there was a continuous increase in ram pressure as the ground was approached for both ground boundary conditions. The fixed ground effect, however, produced a lower C_p on the airfoil's lower surface for $h/c < 15\%$ while a higher C_p than the moving ground for $h/c > 15\%$. The slightly higher C_p of the fixed ground can be attributed to the longitudinal boundary layer developed on the fixed ground surface, which further restricts the flow passage, leading to an increased flow deceleration underneath the airfoil and thus a higher C_l compared to its moving-ground counterpart. The escapement of the high-pressure fluid from the airfoil's lower surface also caused an increased leading-edge suction peak, followed by a reduced suction pressure as compared to the OGE case. The increased $dp/dx > 0$ gradient in the ground effect also led to an earlier flow separation at around $x_{sep}/c = 0.07$, 0.08, 0.09 for $h/c = 5\%$, 10%, and 20% at $\alpha = 8$ deg, respectively, in comparison with $x_{sep}/c \approx 0.1$ of the OGE case (see Figs. 4(*a*)–4(*g*)). Only a marginal difference in x_{sep}/c between the fixed and moving ground effects was noticed at the Reynolds number tested.

Figures 3(*e*) and 3(*f*) also reveal that as α was further increased to, for example, $\alpha = 9$ deg, there was a large drop in the suction pressure for $h/c < 7.5\%$, implying an earlier stall of the airfoil in close ground proximity. Note that a static-stall angle at 10.5 deg accompanied by a large increase in C_d and a maximum C_l were obtained outside the ground effect. In ground effect, the drop in the suction pressure was, however, accompanied by a continuous C_l increase.

The fixed ground effect-produced lower C_l in close ground proximity can be related to the ground vortex, or recirculation flow, developed underneath the airfoil's leading edge (Figs. 4(*e*)

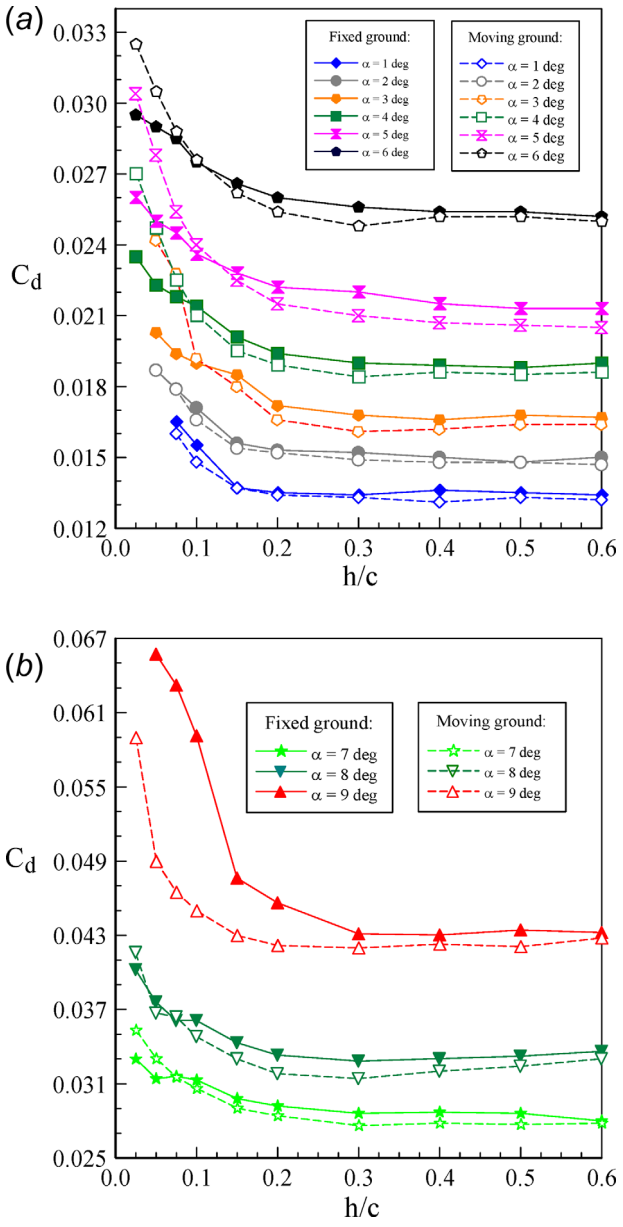

Fig. 8 Ground effect on C_d as a function of α and h/c. Open and solid symbols denote moving ground and fixed ground, respectively.

and 4(*f*)), which speeded up the flow velocity, leading to a smaller-than-moving-ground C_l. The ground vortex became indiscernible for $h/c > 10\%$. By contrast, no ground vortex appeared for the moving ground condition (Figs. 4(*a*)–4(*c*)). The absence of the ground vortex enabled an increase in the velocity as the flow speeded up to meet the velocity at the ground surface (i.e., with $u_{surface} = U$), causing the flow to remain nearly uniform beneath the airfoil as it approached the moving ground surface. The iso-u/U contour of the baseline airfoil was also included in Fig. 4(*d*) to serve as a comparison. The ground vortex and the flow separation region can be more readily reflected from the streamline patterns and velocity vector plots presented in Figs. 5 and 6.

Figures 5(*a*)–5(*c*) and 5(*e*)–5(*g*) show that, in addition to the appearance and disappearance of the ground vortex in close fixed and moving ground proximity, there was also a downstream movement of the lead-edge stagnation point as compared to the OGE case (Fig. 5(*d*)). The smaller the h/c, the larger the stagnation point movement. The moving ground caused a larger movement of the stagnation point than the fixed ground. The ground effect-produced reduced flow velocity beneath the airfoil (indicative of a higher ram pressure and C_l), earlier upper-surface flow separation, and flow escapement in the airfoil's leading-edge region can be clearly seen in Fig. 6. The flow deceleration underneath the airfoil's leading-edge region was followed by an increased flow in the trailing-edge region, which is in agreement with the C_p distribution discussed in Figs. 3(*c*) and 3(*d*). The iso-v/U contours further indicate that the moving ground effect caused an increased upwash in the airfoil's leading-edge region (Figs. 7(*a*)–7(*c*)) as compared to the fixed ground (Figs. 7(*e*)–7(*g*)). The extent of the upwash increased with reducing h/c.

Now, the impact of ground boundary condition on C_d is evaluated (Figs. 8(*a*) and 8(*b*)). The C_d was found to persistently increase with reducing h/c for all α tested, regardless of the ground boundary condition. The C_d increased considerably with reducing h/c for $h/c < 20\%$. For $h/c > 20\%$, the C_d became less sensitive to the change in h/c. The fixed ground effect, however, produced a slightly higher C_d than the moving ground for $h/c > 10\%$ due to the higher ram pressure while a smaller C_d for $h/c < 10\%$ for $\alpha > 3$ deg. For $\alpha < 3$ deg, only a marginal discrepancy exhibited between the two ground boundary conditions tested. In addition to the drag introduced by the ram pressure, the separated flow region over the airfoil's upper surface and the near wake (see Fig. 9) also contributed to the C_d increase.

Figures 9(*a*)–9(*d*) shows that the ground proximity always caused an increased wake width and deficit for both ground boundary condition at $x/c = 1.125$, 1.25, 1.5, and 2. For clarity, the centerline of the OGE near wake was shifted downward to $y/c = 0.7$. Both wake width and deficit were found to increase with reducing h/c. The wake width continued to increases with increasing x/c while the wake deficit was decreased. The moving ground effect produced a larger wake deficit compared to the fixed ground effect. The larger wake deficit, together with the higher ram pressure, gave rise to a larger C_d of the moving ground than the fixed ground.

At last, the impact of the ground boundary condition on C_l/C_d and C_m at selected α was also summarized in Figs. 10(*a*) and 10(*b*). As can be seen, the moving ground boundary condition produced an increased lift-to-drag ratio, especially in close ground proximity, as compared to the fixed ground for $\alpha > 3$ deg, while a lowered C_l/C_d for $\alpha < 3$ deg (Fig. 10(*a*)). For $\alpha \geq 9$ deg, both ground boundary conditions led to a deteriorated C_l/C_d ratio in comparison with the OGE case. In close ground proximity, there was a large nose-up C_m for $\alpha < 3$ deg while a nose-down C_m for $\alpha > 3$ deg (Fig. 10(*b*)). The maximum $|C_m|$ was found to increase with reducing h/c. For $h/c > 60\%$, the C_m approached the OGE value.

4 Conclusions

The aerodynamic coefficients and flowfield of a NACA 0012 airfoil produced by fixed and moving ground effects were quantified experimentally at $Re = 9.2 \times 10^4$. For both ground boundary conditions, the C_l always increased progressively with reducing ground distance for $\alpha > 3$ deg. In close ground proximity, the C_l was found to increase drastically. For $\alpha < 3$ deg, the C_l became smaller than the OGE value in close ground proximity due to the converging-diverging flow passage developed underneath the airfoil. Both ground boundary conditions led to an earlier flow separation. The C_d was also found to increase continuously with reducing ground distance for all α tested. A large increase in C_d occurred in close ground proximity.

The fixed ground effect, however, produced a higher C_l than the moving ground due to the boundary layer developed on its surface, which further narrowed the flow passage and led to a higher ram pressure than its moving-ground counterpart. As the ground was further approached, the formation of ground vortex on the fixed ground surface accelerated the flow, giving rise to lower C_l than the moving ground. The fixed ground effect also produced a

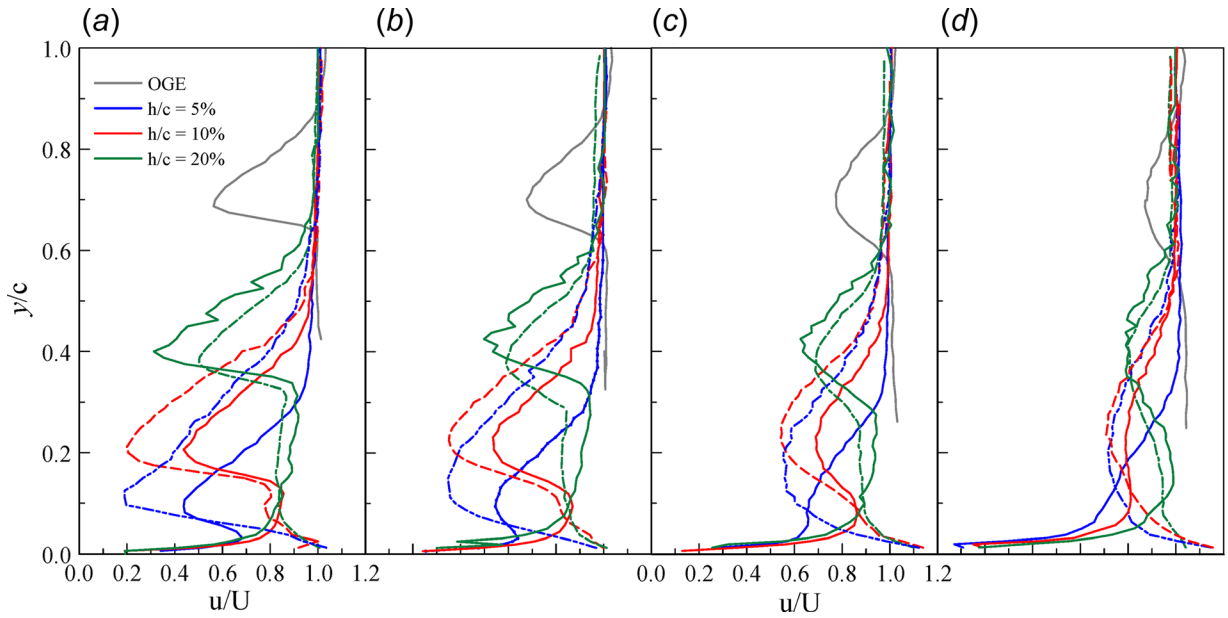

Fig. 9 Near-wake velocity profiles. (*a*) *x/c* = 1.125, (*b*) *x/c* = 1.25, (*c*) *x/c* = 1.5, and (*d*) *x/c* = 2. Solid and dashed lines denote fixed ground and moving ground, respectively.

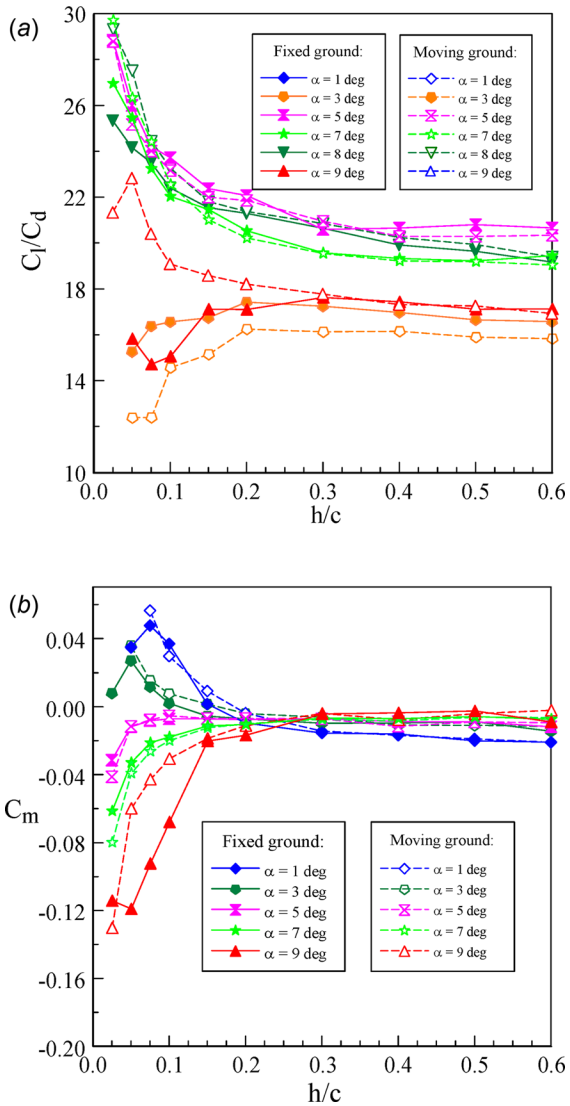

Fig. 10 Variation of (*a*) C_l/C_d and (*b*) C_m with *h/c* at selected α. Solid line denotes fixed ground and dashed line denotes moving ground.

slightly higher C_d near the ground while a considerably lower C_d than the moving ground in close ground proximity. For both ground boundary conditions, the C_d increase was mainly produced by the ram pressure. The flow separation and near wake seem to play a secondary role in the ground effect-induced C_d increase.

Acknowledgment

This work was supported by the Natural Science and Engineering Research Council (NSERC) of Canada.

Nomenclature

AR = aspect ratio
c = chord
C_d = sectional drag coefficient
C_l = sectional lift coefficient
C_m = sectional pitching-moment coefficient
C_p = surface pressure coefficient, $= (p - p_\infty)/{}^1\!/_2\rho U^2$
h = ground distance or clearance
p_∞ = freestream pressure
Re = Reynolds number, $= Uc/\nu$
u,v = streamwise and vertical velocity component
U = freestream velocity
x,y = streamwise and vertical direction
α = angle of attack
α_{ss} = static-stall angle
ν = kinematic viscosity
ρ = fluid density

References

[1] Barber, T. J., Leonardi, E., and Archer, R. D., 2002, "Causes for Discrepancies in Ground Effect Analyses," Aeronaut. J., **106**(1066), pp. 653–667.
[2] Carter, A., 1961, "Effect of Ground Proximity on the Aerodynamic Characteristics of Aspect Ratio-1 Airfoils With and Without End Plates," NASA, Washington, DC, Report No. NASA TN D-970.
[3] Turner, T. R., 1966, "Endless-Belt Technique for Ground Simulation," NASA, Washington, DC, Report No. NASA SP-116.
[4] Suh, Y. B., and Ostowari, C., 1988, "Drag Reduction Factor Due to Ground Effect," J. Aircr., **25**(11), pp. 1071–1073.
[5] Steinbach, D., and Jacob, K., 1991, "Some Aerodynamic Aspects of Wings Near Ground," Jpn. Soc. Aeronaut. Space Sci., **34**(104), pp. 56–70.
[6] Hayashi, M., and Endo, E., 1993, "Measurement of Flowfield Around an Airfoil Section With Separation," Jpn. Soc. Aeronaut. Space Sci., **21**(52), pp. 69–75.
[7] Hsiun, C. M., and Chen, C. K., 1996, "Aerodynamic Characteristics of a Two-Dimensional Airfoil With Ground Effect," J. Aircr., **33**(2), pp. 386–392.

[8] Steinbach, D., 1997, "Comment on Aerodynamic Characteristics of a Two-Dimensional Airfoil With Ground Effect," J. Aircr., **34**(3), pp. 455–456.
[9] Moore, N., Wilson, P. A., and Peters, A. J., 2002, "An Investigation Into Wing in Ground Effect Airfoil Geometry," SCI Symposium on Challenges in Dynamics, System Identification, Control and Handling Qualities for Land, Air, Sea and Space Vehicles, Berlin, Germany, Mar. 13–15, NATO RTO, pp. 11–30, Paper No. RTO-MP-095.
[10] Ahmed, M. R., and Sharma, S. D., 2005, "An Investigation on the Aerodynamics of a Symmetric Airfoil in Ground Effect," Exp. Therm. Fluid Sci., **29**(6), pp. 633–647.
[11] Ahmed, M. R., Takasaki, T., and Kohama, Y., 2007, "Aerodynamics of a NACA 4412 Airfoil in Ground Effect," AIAA J., **45**(1), pp. 37–47.
[12] Luo, S. C., and Chen, Y. S., 2012, "Ground Effect on Flow Past a Wing With a NACA 0015 Cross-Section," Exp. Therm. Fluid Sci., **40**, pp. 18–28.
[13] Qu, Q., Wang, W., Liu, P., and Agarwal, R. K., 2015, "Airfoil Aerodynamics in Ground Effect for Wide Range of Angles of Attack," AIAA J., **53**(4), pp. 1048–1061.
[14] Lee, T., Majeed, A., Siddiqui, B., and Tremblay-Dionne, V., 2018, "Impact of Ground Proximity on the Aerodynamic Properties of an Unsteady Airfoil," Proc. Inst. Mech. Eng., Part G, **232**(10), pp. 1814–1830.
[15] Zerihan, J., and Zhang, X., 2000, "Aerodynamics of a Single-Element Wing in Ground Effect," J. Aircr., **37**(6), pp. 1058–1064.
[16] Zhang, X., and Zerihan, J., 2003, "Aerodynamics of a Double-Element Wing in Ground Effect," AIAA J., **41**(6), pp. 1007–1016.
[17] Han, C., and Cho, J., 2005, "Unsteady Trailing Vortex Evolution Behind a Wing in Ground Effect," J. Aircr., **42**(2), pp. 429–434.
[18] Lee, J., Han, C.-S., and Bae, C.-H., 2010, "Influence of Wing Configurations on Aerodynamic Characteristics of Wings in Ground Effect," J. Aircr., **47**(3), pp. 1030–1040.
[19] Phillips, W. F., and Hunsaker, D. F., 2013, "Lifting-Line Predictions for Induced Drag and Lift in Ground Effect," J. Aircr., **50**(4), pp. 1226–1233.
[20] Zhang, X., and Zerihan, J., 2004, "Edge Vortices of a Double-Element Wing in Ground Effect," J. Aircr., **41**(5), pp. 1127–1137.
[21] Lu, A., Tremblay-Dionne, V., and Lee, T., 2019, "Experimental Study of Aerodynamics and Wingtip Vortex of a Rectangular Wing in Flat Ground Effect," ASME J. Fluids Eng., **141**(11), p. 111108.
[22] Pereira, J., 2011, "Experimental Investigation of Tip Vortex Control Using a Half Delta Shaped Tip Strake," Ph.D. dissertation, Department of Mechanical Engineering, McGill University, Montreal, QC, Canada.
[23] Adrian, R. J., 1991, "Particle-Image Techniques for Experimental Fluid Mechanics," Ann. Rev. Fluid Mech., **23**(1), pp. 261–304.
[24] Raffel, M., Willert, G. E., and Kompenhans, J., 1998, *Particle Image Velocimetry*, Springer, Berlin, pp. 134–146 and 158–160.
[25] Gerontakos, P., and Lee, T., 2008, "PIV Analysis of Flow Over Unsteady Airfoil With Trailing-Edge Strip," Exp. Fluids, **44**(4), pp. 539–556.